J. Fluid Mech. (2010), *vol.* 642, *pp.* 159–180. © Cambridge University Press 2009
doi:10.1017/S0022112009991777

Evolution and decay of a rotating flow over random topography

L. ZAVALA SANSÓN[1]†, A. GONZÁLEZ-VILLANUEVA[2] AND L. M. FLORES[1]

[1]Department of Physical Oceanography, CICESE, Km 107 Carretera Tijuana-Ensenada, 22860 Ensenada, Baja California, México

[2]Colegio de Ciencia y Tecnología, Universidad Autónoma de la Ciudad de México, Prolongación San Isidro 151, San Lorenzo Tezonco, 09790 Iztapalapa, México D.F.

(Received 8 April 2009; revised 20 August 2009; accepted 21 August 2009; first published online 4 December 2009)

The evolution and decay of a homogeneous flow over random topography in a rotating system is studied by means of numerical simulations and theoretical considerations. The analysis is based on a quasi-two-dimensional shallow-water approximation, in which the horizontal divergence is explicitly different from zero, and topographic variations are not restricted to be much smaller than the mean depth, as in quasi-geostrophic dynamics. The results are examined by comparing the evolution of a turbulent flow over different random bottom topographies characterized by a specific horizontal scale, or equivalently, a given mean slope. As in two-dimensional turbulence, the energy of the flow is transferred towards larger scales of motion; after some rotation periods, however, the process is halted as the flow pattern becomes aligned along the topographic contours with shallow water to the right. The quasi-steady state reached by the flow is characterized by a nearly linear relationship between potential vorticity and transport function in most parts of the domain, which is justified in terms of minimum-enstrophy arguments. It is found that global energy decays faster for topographies with shorter horizontal length scales due to more effective viscous dissipation. In addition, some comparisons between simulations based on the shallow-water and quasi-geostrophic formulations are carried out. The role of solid boundaries is also examined: it is shown that vorticity production at no-slip walls contributes for a slight disorganization of the flow.

Key words: geostrophic turbulence, rotating flows, topographic effects

1. Introduction

A homogeneous fluid in a constantly rotating system presents a columnar motion, as derived from the Taylor–Proudman theorem. This behaviour is commonly observed in laboratory experiments in a rotating fluid tank, where columns are parallel to the vertical axis of rotation (for a recent and thorough review see van Heijst & Clercx 2009). The columnar motion of rotating flows is a widely used tool that helps to understand the quasi-two-dimensional behaviour of oceanic and atmospheric flows under the influence of the Earth's rotation (stratification and geometrical considerations related with the shallow-water character of meso- and large-scale geophysical flows are also responsible for its quasi-two-dimensional motion).

† Email address for correspondence: lzavala@cicese.mx

https://doi.org/10.1017/S0022112009991777 Published online by Cambridge University Press

In the absence of external forcing, strictly two-dimensional turbulent flows are characterized by a self-organization process in which energy is transferred from small scales of motion towards larger scales (see e.g. Batchelor 1969). A similar process is observed in quasi-two-dimensional turbulence, where rotation effects and bottom topography variations are taken into account. One of the main differences when variable topography is present, is that the inverse energy cascade is halted as the flow tends towards a steady state, aligned with topography contours with shallow water to the right. This process has been examined in previous papers by Bretherton & Haidvogel (1976), Salmon, Holloway & Hendershott (1976) and Carnevale & Frederiksen (1987), among others, whose analyses are based on the quasi-geostrophic context. The quasi-geostrophic approximation is a valuable tool that helps to understand the behaviour of oceanic and atmospheric flows characterized by time scales larger than the rotation period of the system (i.e. small Rossby numbers) and weak topographic variations (see e.g. Pedlosky 1987).

The main goal of this paper is to study the evolution and decay of a freely evolving flow over variable topography by using a more general shallow-water approximation, in which depth variations are not restricted to be much smaller than the mean depth, as in quasi-geostrophy. By using a rigid-lid approximation, this formulation is essentially (quasi) two-dimensional. However, it allows explicitly a non-zero divergence of the horizontal velocity field, which is due to squeezing and stretching effects of fluid columns as they move over the topography (e.g. Grimshaw, Tang & Broutman 1994). As reported in previous studies, the quasi-two-dimensional approximation is a suitable tool when simulating laboratory experiments with variable bottom topography (see van Heijst & Clercx 2009 and references therein). Furthermore, it might be a more adequate model to study geophysical flows over steep topographic features, such as seamounts, submarine ridges or canyons. The results presented here are obtained by theoretical considerations and numerical simulations based on this physical model. Of course, quasi-geostrophy can be recovered when considering small topographic variations, and therefore some results presented here are closely related with those found in previous studies.

The results are examined for different random topographies, which are characterized by a horizontal length scale or, equivalently, a well-defined mean slope. This provides two important advantages: Firstly, an ensemble of several numerical simulations is performed for a given topographic length scale, so the results are rather general for that type of topography, regardless its random character. Secondly, this procedure allows the comparison of results between topographies with different length scales. Other studies are based on single or few simulations (do not perform ensemble averages) and therefore are not able to make generalizations in terms of the average topography characteristics.

Some properties of the shallow-water system shown here are analogous to their counterparts in quasi-geostrophy. A remarkable one is the above-mentioned tendency to evolve towards a quasi-steady state in which the flow is aligned along topographic contours. Such a flow configuration can be defined in quasi-geostrophy by a functional relationship between potential vorticity and stream function in some parts of the domain, as derived by Bretherton & Haidvogel (1976). These authors proposed a linear relationship by using a variational, minimum-enstrophy principle: the flow evolves towards a state of minimum enstrophy for a given total energy. In the shallow-water model used here, an equivalent relationship between potential vorticity and transport function is verified. The constant of proportionality is a function of the flow energy and it is also related with the characteristic scale of the topography.

https://doi.org/10.1017/S0022112009991777 Published online by Cambridge University Press

Although this linear relation does not strictly hold over the whole domain, it provides a good approximation to the observed flow pattern. A similar variational principle is reported by Adcock & Marshall (2000), who derived an expression for the eddy-induced transport used to parameterize the effect of geostrophic vortices over topography. Even though the present paper is focused on shallow-water dynamics, some comparisons with quasi-geostrophic results are analysed. The procedure mainly consists of comparing numerical simulations based on the two models. Although there are some coincidences in both situations, as expected, there are also clear differences that shall be underlined.

The simulations presented here also explore the influence of boundary conditions when the flow is confined in a square box with solid walls. The role of lateral boundaries in two-dimensional turbulence has been the subject of recent investigations, either numerical or experimental by a number of researchers (e.g. Clercx, Maassen & van Heijst 1999; Maassen, Clercx & van Heijst 2002). These studies have shown that the main effect of solid boundaries is the formation of thin, intense filaments of vorticity that are injected into the flow interior (Clercx *et al.* 2005). Here it shall be shown that the small-scale structures generated at no-slip walls, contribute to decrease the average length scale of the flow or, equivalently, to slightly disorganize the flow. This is achieved by comparing with simulations with free-slip walls.

The organization of the paper is the following. In § 2 the shallow-water model is presented, as well as a minimum enstrophy principle satisfied by the long-term quasi-steady state of the flow. Section 3 describes the numerical parameters used in the simulations and the way to characterize random topographies. Numerical results are presented in § 4, where simulations using different bottom topographies are compared; in addition, different measures for characterizing the flow–topography correlation are proposed. Final remarks and conclusions are included in § 5.

2. Theory

2.1. *Shallow-water model*

Consider a rotating fluid in a Cartesian system with coordinates (x, y), and the axis of rotation parallel to the vertical coordinate z. The evolution equation for the vertical component of the relative vorticity ω is

$$\omega_t + J(q, \psi) = \nu \nabla^2 \omega, \tag{2.1}$$

where ψ is a transport function, subindex t denotes partial time derivative, the horizontal Laplacian is $\nabla^2 = \partial_{xx} + \partial_{yy}$, and $J(A, B) = A_x B_y - A_y B_x$ is the Jacobian operator. The potential vorticity is defined as

$$q = \frac{\omega + f}{h}, \tag{2.2}$$

where f is the Coriolis parameter and $h(x, y)$ is the total fluid depth, which in general depends on the horizontal coordinates (x, y) due to topographic variations, and it is time-independent in the rigid-lid approximation. The continuity equation is

$$(hu)_x + (hv)_y = 0, \tag{2.3}$$

which allows to write horizontal velocities as

$$u = \frac{1}{h}\psi_y, \qquad v = -\frac{1}{h}\psi_x. \tag{2.4}$$

https://doi.org/10.1017/S0022112009991777 Published online by Cambridge University Press

The relative vorticity can be written in terms of the transport function as

$$\omega = -\nabla \cdot \left(\frac{1}{h}\nabla\psi\right),$$
$$= -\frac{1}{h}(\psi_{xx} + \psi_{yy}) + \frac{1}{h^2}(h_x\psi_x + h_y\psi_y). \tag{2.5}$$

In the inviscid limit, the quasi-two-dimensional model has similar invariants as in the quasi-geostrophic approximation. Potential vorticity is materially conserved

$$\frac{\mathrm{D}q}{\mathrm{D}t} = 0, \tag{2.6}$$

with $\mathrm{D}/\mathrm{D}t = \partial_t + u\partial_x + v\partial_y$. In addition, integral quantities such as energy and potential enstrophy are globally conserved. Given the spatial variation of bottom topography it is convenient to write these expressions in terms of volume integrals. The total energy is

$$E = \frac{1}{2}\int \frac{1}{h^2}|\nabla\psi|^2 h \,\mathrm{d}x\,\mathrm{d}y. \tag{2.7}$$

This expression can be rewritten, after standard mathematical steps, as

$$E = -\frac{1}{2}\int \omega\psi \,\mathrm{d}x\,\mathrm{d}y, \tag{2.8}$$

that is, in a similar form as it is usually written in two-dimensional turbulence. However, it must be recalled that units of ψ are different here or, in order to obtain an expression with units of squared velocity, (2.7) has to be divided by the total volume $V = \int h(x, y)\,\mathrm{d}x\,\mathrm{d}y$. The potential enstrophy is defined as

$$Q = \frac{1}{2}\int q^2 h \,\mathrm{d}x\,\mathrm{d}y. \tag{2.9}$$

Both quantities are conserved in the inviscid limit, i.e. $\mathrm{d}E/\mathrm{d}t = \mathrm{d}Q/\mathrm{d}t = 0$ for $\nu \to 0$. There is actually an infinite set of invariants given by the so-called generalized enstrophy, $\int G(q)h\,\mathrm{d}x\,\mathrm{d}y$, where G is an arbitrary, differentiable function of q. It must be noticed that conservation laws for the shallow-water dynamics are equivalent to the corresponding expressions in the quasi-geostrophic model; global functionals, however, are integrated over a volume instead of an area. Potential vorticity conservation implies a potential enstrophy cascade towards smaller scales of motion, according with vorticity elongation arguments: a closed material circuit is strained by the flow while preserving its interior area and the corresponding potential vorticity of interior elements; the continuous elongation and folding of this area represents a transfer of enstrophy to smaller scales of motion (Bretherton & Haidvogel 1976).

The quasi-geostrophic model can be recovered when considering topographic variations much smaller than the total fluid depth. This can be derived by writing fluid depth as $h(x, y) = H - \Delta h(x, y)$, where H is the mean depth, and small deviations are such that $|\Delta h(x, y)| \ll H$. The vorticity equation has the same form as (2.1) but with potential vorticity defined as $q^{qg} = \omega + f\Delta h/H$ and the stream function as $\psi^{qg} = \psi/H$. Note that units of these two fields are different from their counterparts in the quasi-two-dimensional model; using length and time scales, L and T, respectively, it is verified that

$$[\psi^{qg}, q^{qg}] = (L^2T^{-1}, T^{-1}), \qquad [\psi, q] = (L^3T^{-1}, L^{-1}T^{-1}). \tag{2.10}$$

https://doi.org/10.1017/S0022112009991777 Published online by Cambridge University Press

The corresponding expression of the relative vorticity in terms of the stream function is the Poisson equation $\omega = -\nabla^2 \psi^{qg}$. Another difference is that the horizontal velocity has zero divergence, and therefore the velocity components are $u = \psi_y^{qg}$ and $v = -\psi_x^{qg}$.

2.2. *Steady states and minimum enstrophy principle*

A remarkable property of two-dimensional flows is the tendency to evolve towards preferred states of motion as (inverse) energy and (direct) enstrophy cascades take place. When the flow tends to acquire a steady state, nonlinear terms are no longer acting, that is,

$$J(q, \psi) = 0. \tag{2.11}$$

The immediate consequence is that the potential vorticity has the form

$$q = F(\psi), \tag{2.12}$$

where F is a single-valued function at least along each closed streamline. In general F might be nonlinear.

Here it is shown that a linear $q - \psi$ relationship is obtained by deriving a minimum enstrophy principle. An equivalent condition was originally reported by Bretherton & Haidvogel (1976) for the quasi-geostrophic approximation. Consider the state achieved by the flow as one of minimum potential enstrophy given a fixed energy. This variational principle can be formulated as

$$\delta Q + \mu \delta E = 0, \tag{2.13}$$

where μ is a Lagrange multiplier. Using expressions (2.7) and (2.9), and after some manipulations when calculating variations of functionals E and Q, yields

$$\int \nabla \cdot \left[\frac{1}{h} \nabla (q + \mu \psi) \right] \delta \psi \, \mathrm{d}x \, \mathrm{d}y = 0. \tag{2.14}$$

A sufficient condition to satisfy this integral is by demanding

$$q + \mu \psi = q_0, \tag{2.15}$$

where q_0 is a constant, and the slope μ defines a length scale

$$l_b = \frac{1}{\mu^{1/4}}. \tag{2.16}$$

The structure of the quasi-steady state can be anticipated depending on the considered horizontal length scale of the flow L compared with l_b. To see this, (2.15) is rewritten in non-dimensional terms

$$\epsilon \omega' + 1 + \mu H^2 L^2 \epsilon \psi' h' = q_0 H f^{-1} h', \tag{2.17}$$

where $\epsilon = U/fL$ is the Rossby number defined with the velocity scale U. For small scales $L \ll \mu^{-1/4}$,

$$\epsilon \omega' + 1 \sim q_0 H f^{-1} h', \tag{2.18}$$

or in dimensional terms

$$\omega \sim q_0 h - f. \tag{2.19}$$

This means that for relatively small scales the vorticity field resembles the topography. Another limit is when $\mu H^2 L^2 \epsilon \sim 1$, which corresponds to large scales since $L \gg \mu^{-1/4}$ as the flow decays ($\epsilon \to 0$). In this case

$$1 + \mu H^2 L^2 \epsilon \psi' h' \sim q_0 H f^{-1} h', \tag{2.20}$$

https://doi.org/10.1017/S0022112009991777 Published online by Cambridge University Press

which in dimensional terms implies

$$\psi \sim \frac{q_0}{\mu} - \frac{f}{\mu h}. \tag{2.21}$$

Thus, for large scales the transport function (the flow pattern) is inversely proportional to the depth field. This behaviour is observed in the numerical simulations presented in next sections.

Both limits for small and large scales are analogous to those found by Bretherton & Haidvogel (1976) in the quasi-geostrophic context, which can be recovered by using suitable approximations for small topographic variations (and considering that they defined the stream function with opposite sign). The minimum enstrophy principle in quasi-geostrophy is

$$q^{qg} = \mu^{qg}\psi^{qg}, \tag{2.22}$$

where μ^{qg} defines a length scale $l_b^{qg} = 1/(\mu^{qg})^{1/2}$. The equivalence between Lagrange multipliers is derived from (2.15) when the topographic amplitudes are much smaller than the mean depth H:

$$\mu^{qg} = \mu H^2, \tag{2.23}$$

for which $q_0 \approx f/H$ was used (this last approximation is valid only for the quasi-geostrophic limit). Furthermore, the Lagrange multiplier depends inversely on the energy of the flow as (Bretherton & Haidvogel 1976)

$$\mu^{qg} \approx \frac{Sf}{UH}, \tag{2.24}$$

where S is the mean topographic slope. Combining (2.23) and (2.24) in (2.16), the length scale l_b from the shallow-water model can be written as

$$l_b = \left(H l_b^{qg}\right)^{1/2} = \left(\frac{UH^3}{Sf}\right)^{1/4}. \tag{2.25}$$

This expression shall be evaluated when making some comparisons between the two formulations.

3. Methods

3.1. *Numerical parameters*

The dynamical model represented by (2.1) and (2.5) is solved by means of a finite differences code. Time advance in (2.1) is performed by using a third-order Runge–Kutta scheme. The relation between relative vorticity and transport function, (2.5), is solved by using a multigrid method. Bottom friction effects are not considered. The flow–topography correlation, however, is also observed when Ekman friction is included, as shown in Zavala Sansón (2007). The horizontal domain is a 1×1 box divided by a 256×256 square grid. The Coriolis parameter is $f = 1$, corresponding with a rotation period of about $T = 4\pi/f \approx 12.5$. The time step is 0.4 and the duration of the experiments is 1800 ($\sim$150 rotation periods). No-slip boundary conditions are prescribed at the lateral walls, where ψ is set to zero. A comparison with stress-free conditions is shown in the last part of next section.

The initial condition is an array of 16×16 Gaussian vortices with diameter $a = 0.05$ and alternate-sign vorticity with maximum magnitude $|\omega_{max}| = 1$. The array is centred at the square domain. Within a space of length a between the closest row (column)

https://doi.org/10.1017/S0022112009991777 Published online by Cambridge University Press

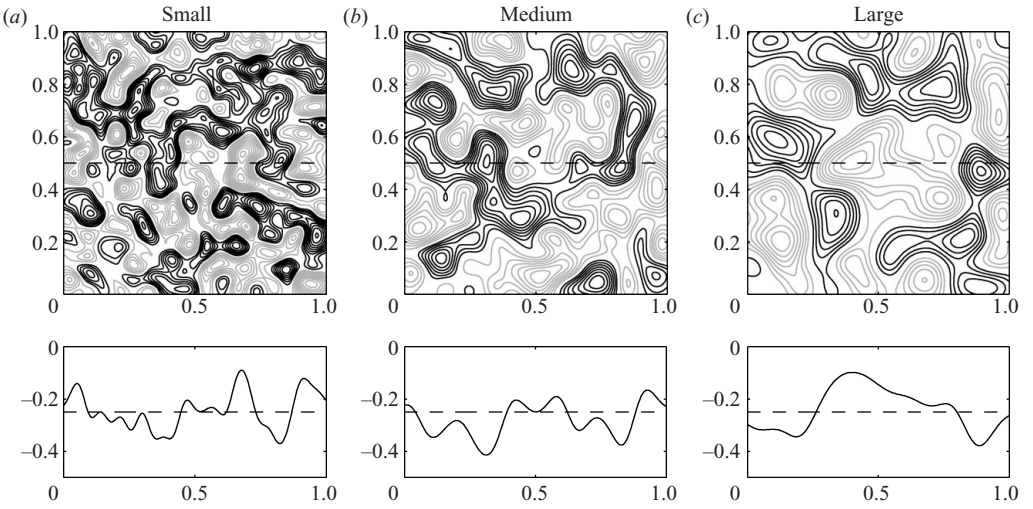


FIGURE 1. Contours of representative bottom topographies $h(x, y) - H$ $(H = 0.25)$ with horizontal length scales (a) small, (b) medium and (c) large. Positive contours are plotted with black lines and represent topographic valleys with respect to the mean value; similarly, negative contours are with grey lines and represent topographic hills. Contour interval is 0.005. The corresponding depth profiles along the horizontal line $(x, 0.5)$ for each topography are shown in the plots below, where the dashed line indicates the mean depth H.

of vortices and the boundaries the vorticity is zero. A similar configuration is used in other studies (Clercx *et al.* 1999; Zavala Sansón & Sheinbaum 2008). The initial positions of the vortices is not uniform in the array, but have a small random perturbation from the vertices. However, the initial positions of the vortices is not relevant, given the random character of the topographies (see below). The Reynolds number based on the initial velocity scale $U = 0.005$, on the initial vortex diameter a, and using $\nu = 10^{-6}$ is $Re = 250$ (Clercx *et al.* 1999 used the half length of the domain, 0.5, which gives $Re = 2500$).

3.2. *Bottom topographies*

Three types of bottom irregularities are analysed, characterized by a specific mean horizontal scale that is much smaller than the domain size. Hereafter, the topographies will be referred to as small, medium and large according to figure 1, which shows one particular topography for each horizontal scale and the corresponding depth profile along the central part of the domain. In all cases the mean fluid depth is $H = 0.25$ and maximum variations are of order ± 0.20. The topographies can be identified by their mean slope $\overline{|\nabla h|}$ (averaged over the hortizontal area), which are 2.26, 1.41 and 1.09, respectively. Of course, the larger the horizontal scale the lower the mean slope. All topographies show a Gaussian distribution, i.e. probability density functions of the depth fields over the whole domain have this distribution. In order to obtain representative results, ensemble averages are calculated with five realizations for each type of topography. It is important to remark, therefore, that the conclusions obtained in this study are derived from several simulations with completely different topographies with common statistical features.

The depth field is generated by superposing a set of Gaussian functions centred at a squared grid mn that is coarser than the domain ij grid, and with amplitudes $\hat{h}_{mn}$

https://doi.org/10.1017/S0022112009991777 Published online by Cambridge University Press

randomly chosen between −0.10 and 0.10. Thus, the depth field is defined as

$$h_{ij} = H + \sum_{mn} \hat{h}_{mn} \exp\left(-r^2_{\{ij-mn\}}/s^2\right), \tag{3.1}$$

where the random amplitudes are defined over the coarse grid, and $r_{\{ij-mn\}}$ is the radial distance of the ij node to the nm nodes. In order to construct three different depth fields, the parameter s is given values of 0.04, 0.06 and 0.08, for the small, medium and large topography, respectively. The corresponding grid size mn is of 25×25, 16×16, and 12×12 points, respectively. Each realization of the ensembles is defined by a different set of random Gaussian amplitudes in (3.1). The depth fields could also be defined in terms of Fourier components $h(x, y) = \sum_{kl} \hat{h} \cos(kx + ly + \hat{\phi})$ with random amplitudes and phases, or with any other approximation. The final results should be the same, since they depend on the average characteristics of the topography.

4. Results

4.1. *Flow evolution*

Figure 2 presents the evolution of the vorticity field calculated in a typical run with a small topographic horizontal scale. The initial condition is shown in figure 2(*a*), and the depth field is in figure 2(*d*). There is an initial stage up to about $t \approx 15T$ (not shown) during which the flow is rather irregular: the main interactions are between vortices, either merging when being of equal sign or translating as dipoles when having different circulation. Larger vortices are then formed, according with the inverse energy cascade. Another important feature is the interaction of vortices with the no-slip wall, forming filaments of opposite sign vorticity, which are injected towards the interior of the domain. At $t \approx 19T$ the influence of the topography becomes evident: the vorticity field has adopted the form of the bottom (figure 2*b*). Fluid columns with positive (negative) vorticity are located over deep (shallow) regions. This configuration is maintained during the rest of the simulation as the flow decays. An additional process after long time periods is that such a distribution does not decay uniformly along the domain. This is clearly observed at $t \approx 76T$ (figure 2*c*): the flow experiences a stronger decay at the domain periphery. This is a first indication of the effect of the no-slip boundaries. Basically, the filaments formed at the walls are constricted to be very thin, according with the scale of the topography, and therefore are rapidly dissipated by viscosity. This effect is further discussed and measured below.

The general behaviour just described is observed for flows over any topographic configuration. Figure 3 presents the contours of potential vorticity, relative vorticity and transport function at $t \approx 67T$, in a simulation with a medium topography field, shown in figure 3(*d*). There are several comparisons that can be made between different figures. For instance, it can be noticed that relative vorticity (figure 3*b*) adopts the shape of the topography for small scales, as indicated by (2.19). In contrast, the transport function (figure 3*c*) is smoothed out or coarser over the whole domain, as expected from (2.21) for larger scales. Potential vorticity (figure 3*a*) is anticorrelated with the topography, since the decaying flow implies that $\omega \ll f$ and therefore $q \to f/h$. In other words, shallow areas correspond with high potential vorticity values, and deep areas correspond with low potential vorticity values. It can also be noticed that potential vorticity tends to be proportional to minus the

https://doi.org/10.1017/S0022112009991777 Published online by Cambridge University Press

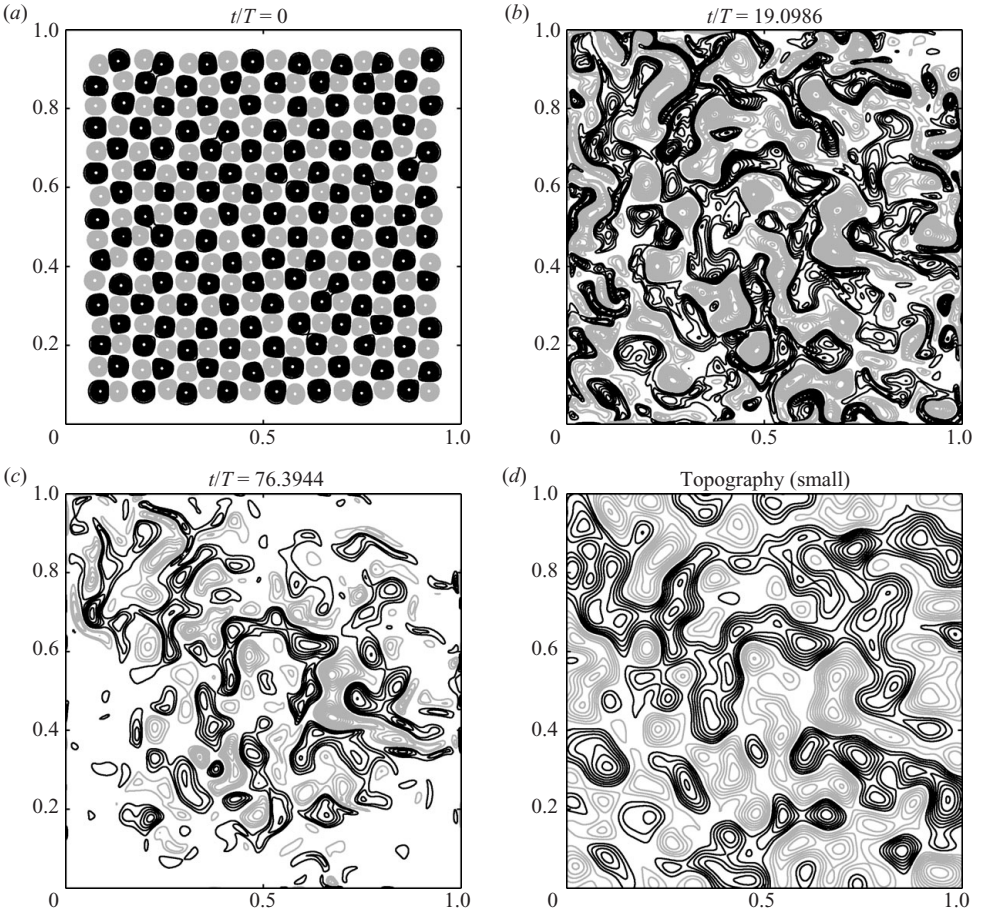


FIGURE 2. Relative vorticity contours calculated at three different times over a small-scale topography (panel *a* shows the initial condition). Positive contours are plotted with black lines, and negative are with grey lines. Contour intervals are 1/10 of maximum vorticity at each time. (*d*) Contours of topography as in figure 1.

transport function (compare figures 3*a* and 3*c*), as expected from the analysis shown in § 2.

All these comparisons are quantitatively discussed in next subsections. More importantly, these observations and some other properties of the flow (such as scatter plots) are measured as a function of the horizontal scale of the topography. This shall be done by performing sets of simulations for each bottom configuration, in order to compute ensemble averages.

4.2. *Evolution of integral quantities*

The most relevant global functionals are the energy and potential enstrophy since their values are conserved for non-viscous flows. Their time evolution is examined in figure 4 by performing ensemble averages for each type of topography. Values are normalized with respect to their initial value. Consider first the evolution of global energy (figure 4*a*). The decay over the three topographies is identical up to times of about $\approx 15T$, which is the initial stage when the flow is governed by vortex interactions. More importantly, for longer times energy decays faster on the small-scale

https://doi.org/10.1017/S0022112009991777 Published online by Cambridge University Press

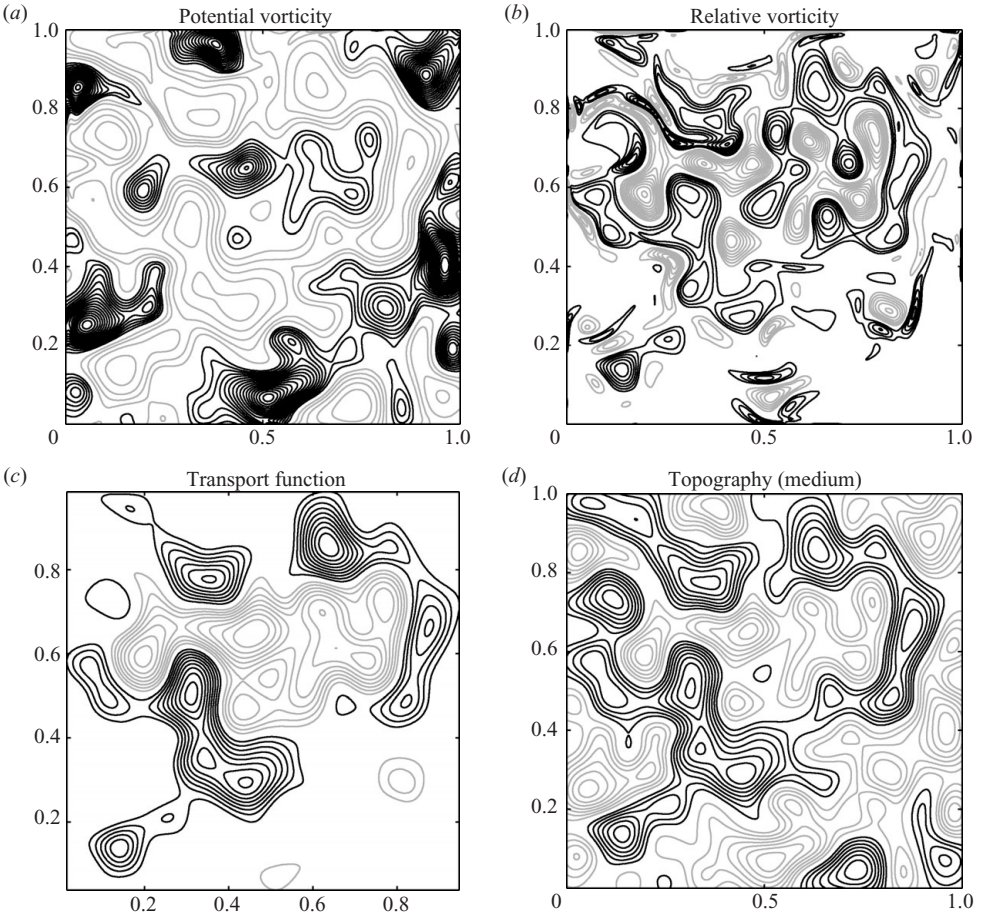


FIGURE 3. Contours of (*a*) potential vorticity $q - \overline{q}$ (with $\overline{q}$ the average value over the whole domain), (*b*) relative vorticity and (*c*) transport function of a flow over a medium-scale topography at time $t/T = 85.94$. Positive contours are plotted with black lines, and negative are with grey lines. Contour intervals are 1/30, 1/30 and 1/10 of maximum values of each field, respectively. (*d*) Contours of the depth field as in figure 1.

topography than on larger scales. The reason for this behaviour is associated with the fact that the flow has adopted the shape of the topography, and therefore dissipation effects due to viscosity are more efficient on shorter length scales. In other words, a smaller local Reynolds number can be associated, implying a more effective viscous dissipation. Thus, the decay rate of energy is influenced by the characteristic length scale of the bottom, which imposes a limitation on the size of vortical structures during the self-organization process. Potential enstrophy also shows a rapid decay until $15T$, nearly identical over any topography (figure 4*b*). After reaching a minimum value, it slightly grows towards a constant value.

The flow organization (or disorganization) can be measured by calculating the time evolution of an integral scale of motion defined with the help of integral functionals. In two-dimensional turbulence one can define $l = (E^{2D}/Z^{2D})^{1/2}$, using the integral energy E^{2D} and enstrophy Z^{2D} in two dimensions (or the equivalent squared wavenumber $k^2 = Z^{2D}/E^{2D}$, Clercx *et al.* 1999). Considering units of potential enstrophy in the

https://doi.org/10.1017/S0022112009991777 Published online by Cambridge University Press

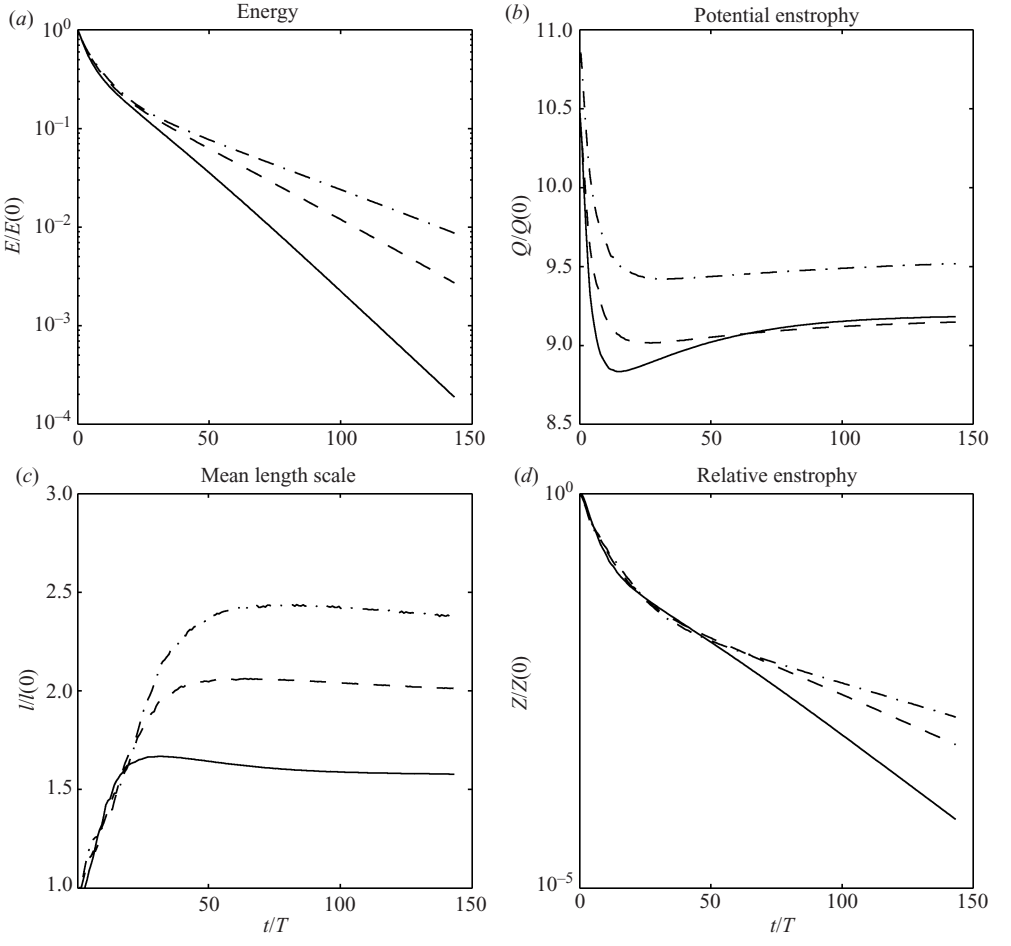


FIGURE 4. Time evolution of (*a*) total energy, (*b*) potential enstrophy, (*c*) average horizontal length scale and (*d*) two-dimensional potential enstrophy calculated from ensemble averages for each topography: small (solid); medium (dashed) and large (dashed-dotted).

shallow-water model one might be tempted to estimate an integral length scale as $l=(E/Q)^{1/4}$. However, this scale is not appropriate since after long times Q scales as $(f/H)^2/2$, that is, the length scale of motion (associated with the flow) is lost. Instead, the relative enstrophy now integrated over the whole volume $Z=1/2\int\omega^2 h\,\mathrm{d}x\,\mathrm{d}y$ can be used to define

$$l=\sqrt{\frac{E}{Z}}. \tag{4.1}$$

This scale is associated with the flow organization: it is expected to observe l to increase in time when starting from values smaller than the horizontal topographic scale, as in all cases studied here. The corresponding curves for the three topographies are shown in figure 4(*c*) (figure 4*d* shows the decay of relative enstrophy, which is rather similar in all cases). As for the case of energy, during initial stages this scale has a very similar increase over any topography. This behaviour is produced as the flow adopts the shape of the topography. The time at which the growth rate changes can be considered as a measure of the time lapse when the inverse cascade takes

https://doi.org/10.1017/S0022112009991777 Published online by Cambridge University Press

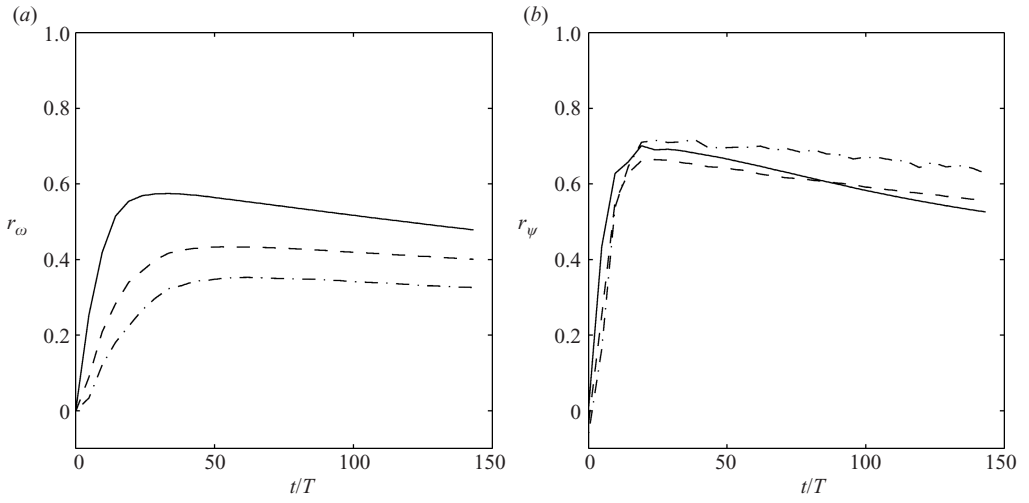


FIGURE 5. Time evolution of the normalized, two-dimensional cross-correlation coefficients (*a*) r_ω and (*b*) r_ψ, for each topography: small (solid); medium (dashed) and large (dashed-dotted). Note that in all cases correlations are nearly zero at $t = 0$, when the initial flow is uncorrelated with the topography.

place, which is longer for larger topographic scales. This interval is about 15, 25 and 30 rotation periods for the small, medium and large-scale topographies, respectively. At a certain time l reaches a maximum, which, again, occurs first for the small-scale bottom. For later stages a slight decay is observed. This effect is partially due to the influence of the walls: the short scale of the thin filaments ejected from the walls contribute to decrease the value of l.

A quantitative expression of the flow–topography alignment can be calculated by means of the two-dimensional cross-correlation coefficient r between these two fields. For two square matrices $\boldsymbol{A}$ and $\boldsymbol{B}$ with dimensions N, the equation for the normalized, zero-lag cross-correlation is

$$r(t) = \frac{1}{N-1} \sum_{ij} \frac{(A_{ij} - \overline{A})(B_{ij} - \overline{B})}{\sigma_A \sigma_B}, \tag{4.2}$$

where $\overline{A}$, $\overline{B}$, σ_A and σ_B are the corresponding mean values and standard deviations. The correlation coefficient is a function of time as the flow evolves over the topography. There are two ways to calculate this parameter by using (2.19) and (2.21), which result in coefficients $r_\omega(t)$ and $r_\psi(t)$. The first one, r_ω, measures the correlation between relative vorticity ω and the topography using (2.19), while r_ψ compares the transport function ψ with the inverse of the depth field using (2.21). Figure 5 shows the time evolution of the corresponding coefficients calculated with ensemble averages for each topography (average values of μ and q_0 are used for each case). Initially, the coefficients are very close to zero, since the initial flow is nearly uncorrelated with the depth field. The correlations are increased as the flow evolves and adapts to the shape of the topography. Coefficients r_ω (figure 5*a*) have a regular behaviour for the three topographies: they increase in time, as expected, and reach a maximum after which all of them slightly decay, especially for the small topography. The correlation increases faster and is larger for smaller topographies. Coefficients r_ψ (figure 5*b*) do not allow a

https://doi.org/10.1017/S0022112009991777 Published online by Cambridge University Press

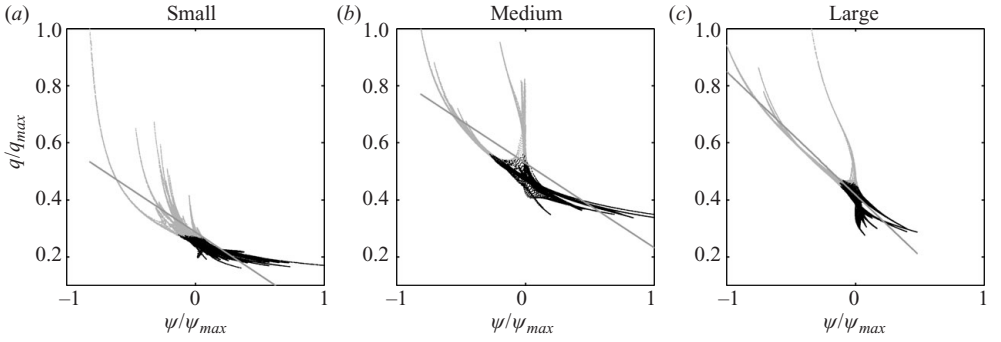


FIGURE 6. Scatter plots calculated at time $t/T = 86$ for flows over three different bottom topographies: (*a*) small, (*b*) medium and (*c*) large. Superposed straight lines are the least-square fit in each case. Potential vorticity and transport function are normalized with maximum values. Dark points correspond with valleys and grey points correspond with hills with respect to the mean depth.

clear distinction between the different topographies. For these reasons, coefficients r_ω are a more valuable tool for quantitatively measuring the flow–topography alignment.

4.3. *Scatter plots*

The relationship between potential vorticity and transport function is analysed by means of scatter plots. The intention is to verify to what extent a functional relationship between these two fields exists, and how far is from being linear, as expected from minimum-enstrophy arguments. Scatter plots constructed with local values of q and ψ are shown in figure 6 (points within a narrow area next to the walls are not considered in order to exclude the influence of the boundaries; when these points are included the results are very similar). Typical results for the three different topographies are presented at $t = 86T$, when the flow is well aligned with the topography in all cases. The diagrams show a set of branches that represent areas where there is a relatively well-defined $q - \psi$ functional relation. These regions mainly correspond with submarine mountains or canyons, either separate or together. Therefore, the small-scale topography presents a larger number of such branches, since in average there are more topographic irregularities. Note that dark (grey) points correspond to topographic depressions (bumps). Then, as expected, structures with positive circulations ($\psi > 0$) are located over valleys, while negative circulations ($\psi < 0$) correspond with hills.

Another remarkable feature observed in scatter plots is that the slope of the structures with positive circulations is smaller than those with negative values, specially for the small topography. Besides, the $q - \psi$ relationship might or might not be linear in specific locations. Figure 7 shows two examples. First, consider a particular area comprising both a mountain and a valley from a medium-size topography (figures 7*a* and 7*b*). Recall that over these topographic features there is negative relative vorticity over the mountain and positive over the valley. Evidently, the slope of the points over the hill is larger than that of the points over the valley. The $q - \psi$ relation here is clearly nonlinear, although the tendency is similar in the sense that $\mathrm{d}q/\mathrm{d}\psi < 0$. The $q - \psi$ relationship might look more linear in some cases. This is shown in figures 7(*c*) and 7(*d*) for the case of a rectangular area containing a mountain and a valley from a large-scale topography (the coarser case). The points

https://doi.org/10.1017/S0022112009991777 Published online by Cambridge University Press

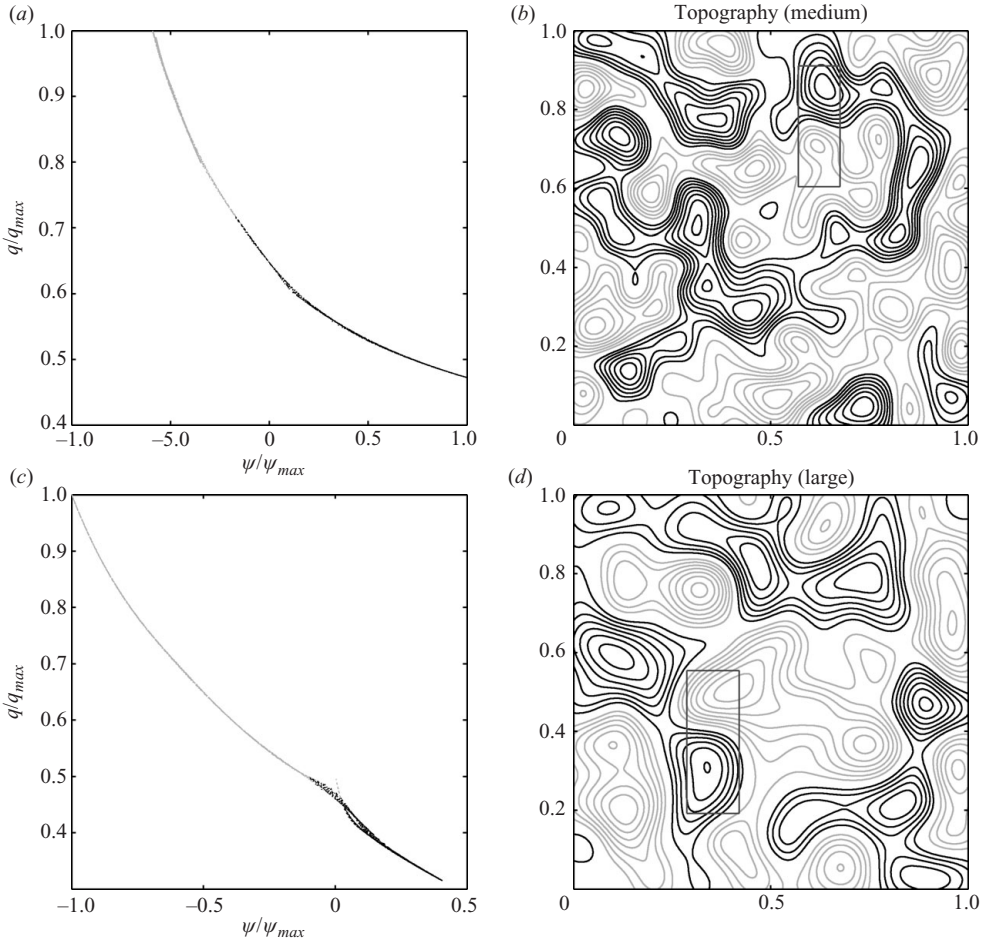


FIGURE 7. Scatter plots calculated at time $t/T = 86$ using data points inside limited rectangular areas covering both a deep and shallow regions. (a) and (b): Rectangular area in a medium topography. (c) and (d): Rectangular area in a large topography. Potential vorticity and transport function are normalized with maximum values. Dark points correspond with valleys, and grey points correspond with hills with respect to the mean depth. Topography contours as in figure 1.

that most deviate from the linear relationship are those where ψ changes sign, i.e. at the region between the mountain and the valley.

Since the configuration of the scatter plot is strongly dependent on the specific shape of each topography, it is useful to determine a quantitative measurement that distinguishes the results between topographies with different length scales. This can be done by assuming that a linear $q - \psi$ relationship is valid over the whole domain. In figure 6 a least-squares best fit corresponding to $q = -\mu\psi + q_0$ is also shown in the scatter plots (solid line). Recall that the corresponding slope μ gives a length scale $l_b = \mu^{-1/4}$. Furthermore, as the flow continues its decay there are changes in the value of the Lagrange multiplier, and hence l_b is also time dependent. Therefore, its evolution can be calculated by fitting a linear $q - \psi$ relationship at different times. This procedure can be applied to the whole ensemble of simulations for each topography and take the corresponding average values. This is presented in figure 8(a), where

https://doi.org/10.1017/S0022112009991777 Published online by Cambridge University Press

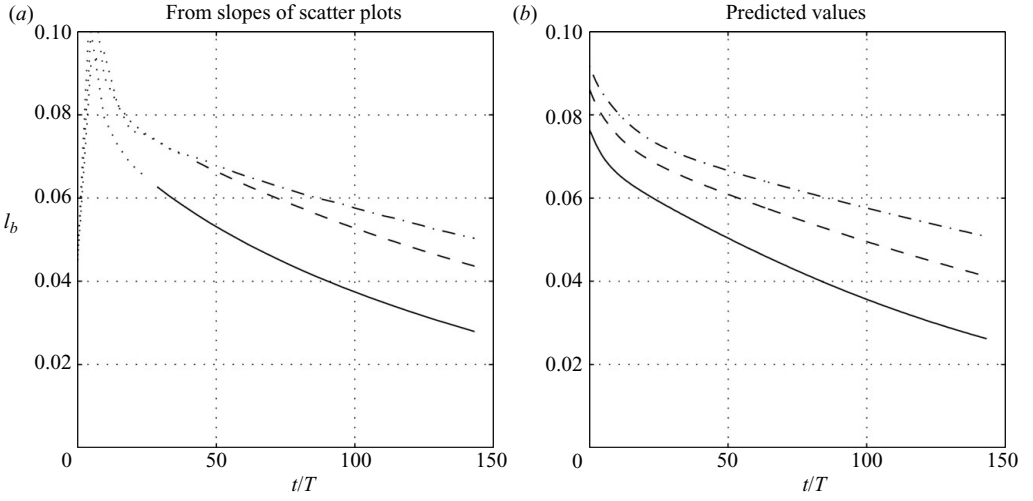


FIGURE 8. Time evolution of the length scale l_b for each topography: small (solid); medium (dashed) and large (dashed-dotted). (a) Calculated from scatter plots of each one of the five simulations for each topography and ensemble averaged; values are measured every five rotation periods; initial values (dotted) are not valid. (b) Predicted values from expression (2.25), using $U \approx 2\sqrt{E}$, where E is the total energy of the flow measured from the ensembles of shallow-water simulations.

the time evolution of l_b is computed for the three topographies. Values during the first rotation periods are not shown since at these times the flow has not clearly acquired the shape of the topography and therefore the linear fit does not have sense. The three curves show that l_b decreases in time, with coarser topographies having larger magnitudes. This result can be compared with the predictions given by expression (2.25), which basically gives the dependence of l_b with the decaying velocity scale of the flow U. Using $U \approx (2E)^{1/2}$ measured from the simulations, the predicted values for l_b (ensemble averaged) can be estimated. These are shown in figure 8(b). The resemblance with the directly measured curves is evident. Recall, however, that the theoretical values (2.25) are derived with the help of quasi-geostrophic results. This is a first indication on the relation between both formulations, despite the abrupt topographies studied here. In next subsection a more systematic comparison is explored, showing more coincidences and differences between the two dynamical models.

4.4. *Some comparisons with quasi-geostrophy*

The scope of this paper is to describe quantitatively the flow–topography adjustment in the shallow-water formulation, which is more ample than the quasi-geostrophic theory. Nevertheless, it is useful to investigate some comparisons between simulations based on the two formulations. Recall that the range of topographic variations used here is rather wide: there can be hills or valleys with maximum amplitude of about 80 % of the mean depth. Such a range would not be valid for quasi-gestrophic theory, in which bottom features are restricted to be much smaller than the mean depth. Despite this, the simulations presented up to here were repeated under the quasi-geostrophic approximation described in § 2. It must be recalled that instead of a transport function ψ, in the quasi-geostrophic case a stream function ψ^{qg}, with

https://doi.org/10.1017/S0022112009991777 Published online by Cambridge University Press

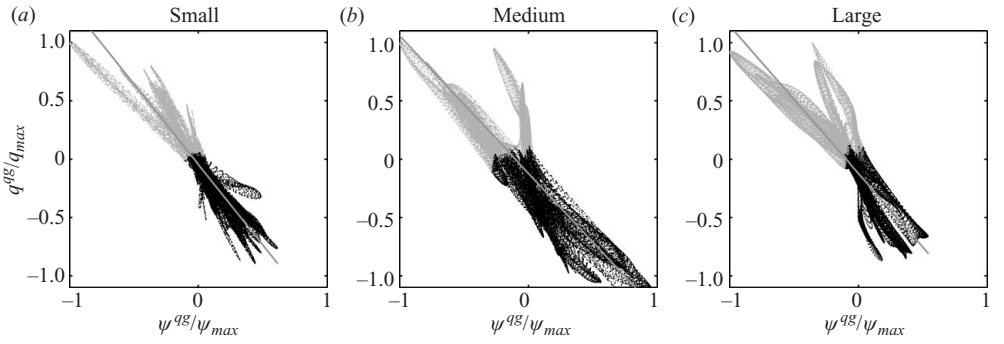


FIGURE 9. Scatter plots calculated from numerical simulations based on quasi-geostrophic dynamics at time $t/T = 86$ for flows over three different bottom topographies: (*a*) small, (*b*) medium and (*c*) large. Plots can be compared with shallow water simulations shown in figure 9.

different units, must be solved. The corresponding potential vorticity is also defined with different units, as shown in (2.10).

A first result is that the main flow characteristics present a similar trend in both formulations (not shown here): the flow acquires the shape of the topography in 10–20 rotation periods, with cyclonic (anticyclonic) circulation over valleys (hills). This qualitative agreement between the shallow-water and the quasi-geostrophic simulations is found for the three different topographies. This is in fact somewhat surprising when considering that the restriction of small topographic amplitudes is clearly violated.

In order to investigate quantitative differences between both formulations, scatter plots from quasi-geostrophic simulations are examined. These are shown in figure 9, which can be compared with the corresponding shallow water plots presented in figure 6. The differences are qualitatively very clear: in the quasi-geostrophic case there is much more dispersion, in contrast with the well-defined branches in the shallow water case that show little dispersion. Another difference is that in quasi-geostrophy the slope of the whole plot is nearly constant for positive or negative circulations, while such a slope is greater for negative ψ values than for positive in the shallow-water model, as described in the previous subsection. Recall that, due to the flow–topography adjustment, the former are mainly points over valleys and the latter are points over hills. The more symmetrical situation in quasi-geostrophy is expected when considering that changes in relative vorticity when climbing or descending the topography are equivalent for cyclonic or anticyclonic fluid columns. In contrast, such changes are different for columns in the shallow water formulation, where they depend on the local fluid depth besides the topographic variation (see also Zavala Sansón 2007).

Another way to make comparisons is by means of the energy decay measured from the ensemble of five simulations for each topography. Recall that the total energy in the quasi-geostrophic case is calculated as

$$E^{qg} = -\frac{1}{2}\int \omega\psi^{qg}\,\mathrm{d}x\,\mathrm{d}y, \tag{4.3}$$

which has the same form as (2.8) but now using the stream function. Equivalently, (4.3) has to be divided by the total area $A = \int \mathrm{d}x\,\mathrm{d}y$ (equal to 1 in the present case) in order to obtain an expression with units of squared velocity. The ratio between shallow water and quasi-geostrophic energies, E/E^{qg}, is shown in figure 10(*a*). It is

https://doi.org/10.1017/S0022112009991777 Published online by Cambridge University Press

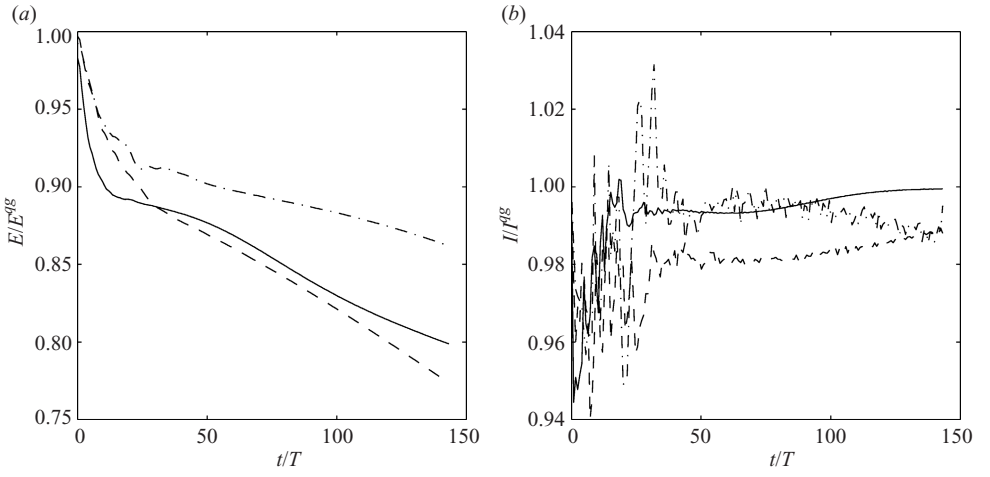


FIGURE 10. Time evolution of global quantities in shallow-water and quasi-geostrophic simulations for each topography: small (solid); medium (dashed) and large (dashed-dotted). (*a*) Ratio of energy E/E^{qg}. (*b*) Ratio of length scales l_b/l_b^{qg}.

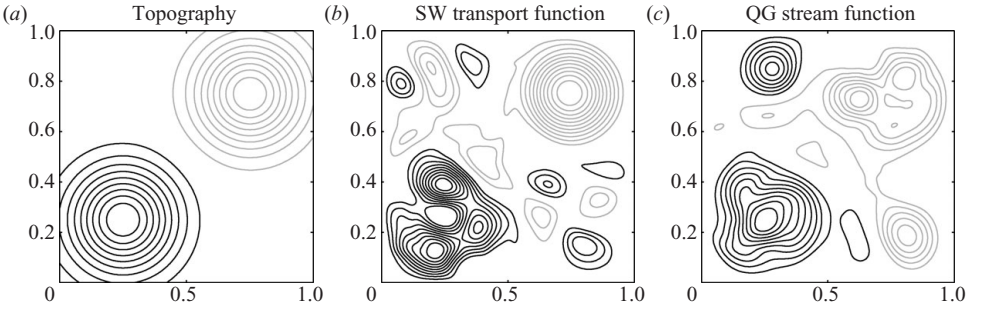


FIGURE 11. (*a*) Topography contours of a Gaussian valley and mountain. Positive contours are plotted with black lines, and negative are with grey lines. Contour interval is 0.005. Relative vorticity contours from (*b*) a shallow-water simulation, (*c*) a quasi-geostrophic simulation. Contour intervals as in figure 2.

observed that in all cases this ratio tends to be smaller than unity, i.e. in average the total energy in the quasi-geostrophic simulations decays slower than in the shallow water model. Note also that there is no clear distinction between the three types of topography, and the three cases show an abrupt decay during the first rotation periods and a slower decay afterwards. In addition, the lenght scale $l^{qg} = (E^{qg}/Z^{qg})^{1/2}$ is calculated, based on the total energy and enstrophy in the quasi-geostrophic domain (area integrals), analogous to expression (4.1). The ensemble averages of the ratio l/l^{qg} are shown in figure 10(*b*). Although the signal is rather noisy, it can be observed that both length scales are very similar during the whole simulations; this indicates that the adjustment of the flow to the topographies is rather similar in both dynamics.

The qualitative similarity between simulations based on shallow-water dynamics and quasi-geostrophy is favoured by the random character of the topography. In other words, it might be broken for larger horizontal scales of the variable topography. Figure 11 presents the case of a topography given by a Gaussian valley and hill as shown in figure 11(*a*). The mean depth is, as in previous cases, $H = 0.25$. The

https://doi.org/10.1017/S0022112009991777 Published online by Cambridge University Press

topographic amplitude is ± 0.2, so the summit of the mountain has 0.05 depth and the deepest point of the valley 0.45. The flow configuration after about 50 rotation periods in simulations based on shallow-water dynamics and quasi-geostrophy are shown in figures 11(b) and 11(c), respectively (using the same initial condition as in the rest of the simulations). For the shallow-water case the transport function is plotted, while the stream function is used for the quasi-geostrophic simulation. Although the flow tends to accumulate cyclonic vorticity over the valley and anticyclonic over the mountain, the qualitative arrangement is clearly different. Similar results have been observed for a number of simplified topographies: single mountains, long ridges among others (not shown). In other studies the differences observed between both models are also remarkable, specially when using single vortices over simple topographies as in Zavala Sansón & van Heijst (2002). In that study, laboratory experiments of unstable vortices were successfully reproduced when using shallow-water simulations, while quasi-geostrophy provided less satisfactory results.

4.5. *Effects of boundary conditions*

No-slip boundary effects play a role in the evolution of the flow as thin filaments are ejected from the walls. This can be anticipated by visual inspection of vorticity plots, which indicate that the flow decay is somewhat faster near the walls. A quantitative measure to validate this assertion consists of comparing the energy decay in the region adjacent to the walls with the energy of an equivalent area in the interior, as shown figure 12(a). Since the boundary and the interior regions have the same area, the initial energy is almost the same (being slightly greater in the interior given the initial condition). The time evolution of the energy at these areas for the different topographies is shown in figure 12(b–d). As expected, the energy in the exterior presents a faster decay. Recall that values presented here are referred to ensemble averages. Note, however, that this effect is more pronounced during initial stages.

In order to investigate further the effect of the boundary conditions, the same sets of five simulations for each one of the three topographies have been repeated but now using free-slip boundaries. The flow evolution in all cases is similar to those in previous figures (not shown here). In other words, the flow organizes along topographic contours, and after several rotation periods it is weakly disorganized. A direct comparison between simulations with no-slip and free-slip boundary conditions is obtained by taking the average of global quantities over the whole set of 15 runs for each case. Figure 13 presents the evolution of the corresponding global variables, now denoted with brackets $\langle\cdot\rangle$, in simulations using both types of boundary conditions. As expected, energy decays slower when using the free-slip condition, since there is no production of thin filaments at the walls (which eventually can be dissipated more efficiently). For the same reason, the mean length scale l grows faster and reaches larger values in the free-slip simulations. Recall that in the no-slip case the formation of these thin structures at the boundaries contribute to diminish this mean value. In this sense, the effect of no-slip lateral boundaries is then, at least partially, to disorganize the decaying flow. The slow decay of l for very long times in the free-slip case is apparently due to the weaker enstrophy decay (see figure 15d).

5. Discussion and conclusions

The behaviour of barotropic flows in a rotating system under the influence of an abrupt variable bottom topography has been analysed in a shallow-water formulation. As in two-dimensional turbulence, the flow has a self-organization tendency due to

https://doi.org/10.1017/S0022112009991777 Published online by Cambridge University Press

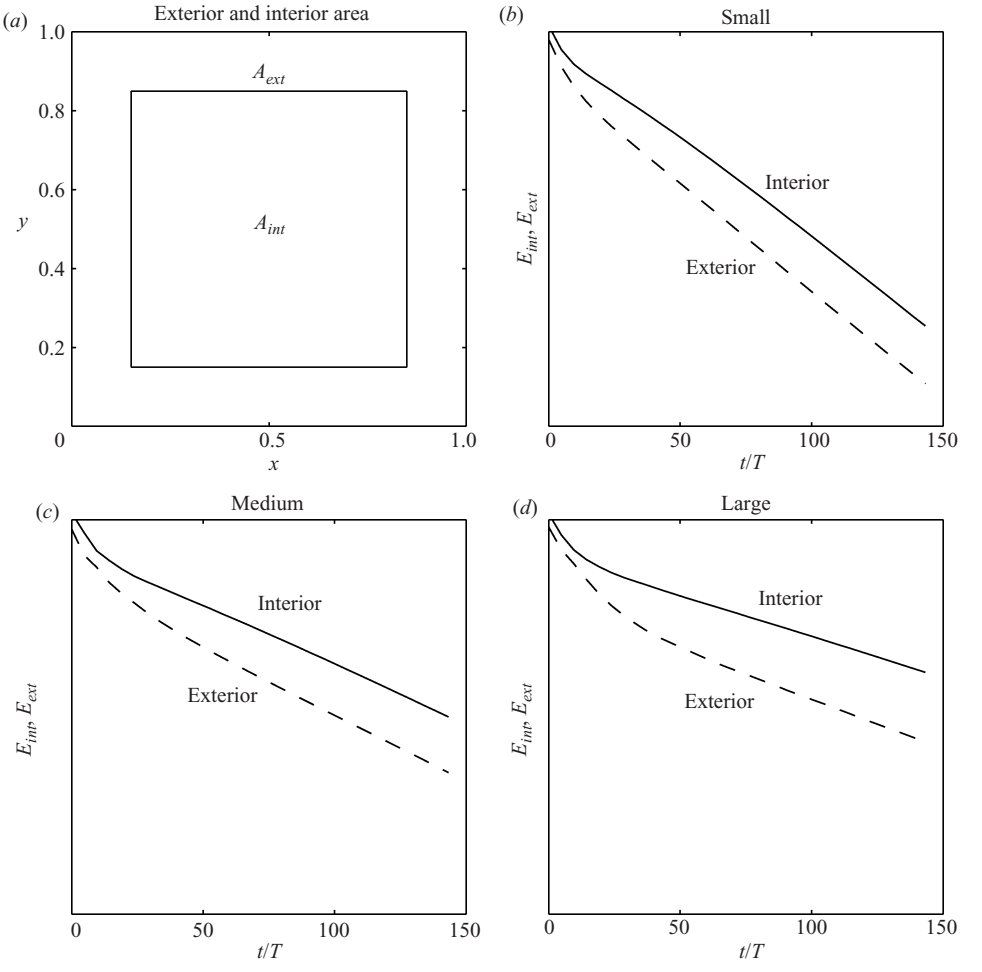


FIGURE 12. (*a*) Definition of interior and exterior regions. The interior square region has length 0.707 and has the same area as the exterior region. (*b*)–(*d*) The time evolution of the energy in the interior (solid) and the exterior (dashed) of the flow domain for the ensembles with different topographies.

an inverse cascade that concentrates energy in larger scales of motion. Such a process is halted after a few rotation periods, as the flow becomes aligned with the contours of topography, i.e. when it reaches the horizontal scale of the topography.

The results are examined in terms of the characteristic horizontal length scale of the topography. For instance, global energy decays faster for smaller topographic scales. This is due to the fact that the maximum length scale that the flow reaches as it becomes aligned with topographic contours is also smaller; therefore, although rather weak, viscous effects are more efficient. This is a robust result based on ensembles of simulations for each topography.

The flow evolution and decay process can be characterized by using two independent measures (see § 4.2). One is the estimate of the global scale of the flow l, which is measured by dividing the total energy and the relative enstrophy of the flow. Such a scale increases in time according with the inverse energy cascade, until the flow has acquired the shape of the topography, at about 15 rotation periods. Afterwards,

https://doi.org/10.1017/S0022112009991777 Published online by Cambridge University Press

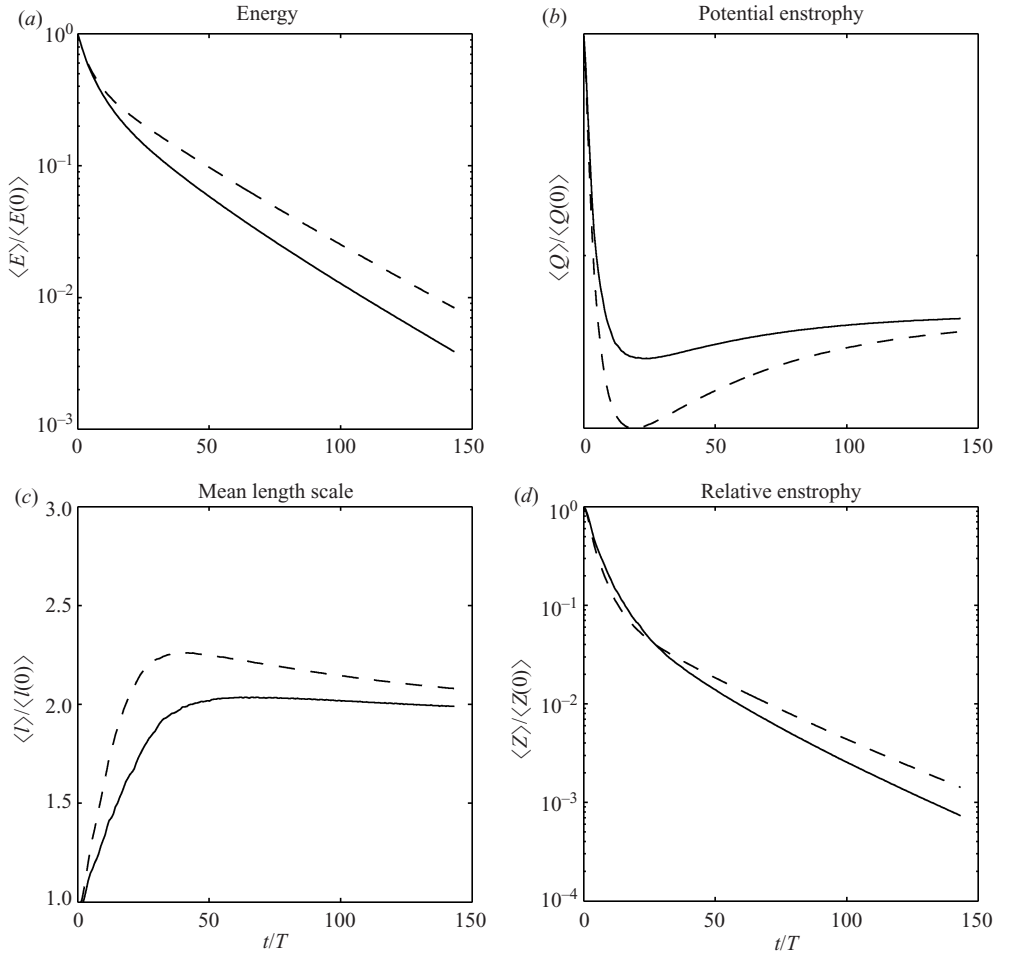


FIGURE 13. Time evolution of global functionals based on ensemble averages over the three types of topographies (15 simulations) using no-slip (solid) and free-slip (dashed) boundary conditions.

a slight decay of l is observed, which indicates a weak disorganization of the flow. Another quantity describing this process is the cross-correlation coefficient r_ω that compares the relative vorticity field with depth anomalies as a function of time. Both measures are obtained from ensemble averages, and therefore their time evolution reliably represent the flow organization–disorganization over each type of topography.

As the flow is aligned with the topography and reaches a quasi-steady state, there is a tendency to develop a well-defined relationship between potential vorticity and transport function, as demanded by $J(q,\psi)\to 0$. Certainly, however, this relation does not hold in all regions, and in some cases does not even exist. From the theoretical point of view, a linear relationship is suggested from a minimum potential enstrophy principle that is satisfied when $q=-\mu\psi+q_0$ (§2). The variational principle is analogous to that derived by Bretherton & Haidvogel (1976), who expressed an equivalent relationship for quasi-geostrophic flows (with different units of q, ψ and the Lagrange multiplier μ). In the present study a further step has been taken by assuming that such a linear relationship is valid over the whole domain, and then

https://doi.org/10.1017/S0022112009991777 Published online by Cambridge University Press

deriving the scale $l_b = \mu^{-1/4}$ for three different random topographies using ensemble averages. Although scatter plots reveal that this relation is linear in some areas and far from linear in some other specific regions, the general trend when considering the whole domain validates this assumption. The key factor by which this theory seems to work is the random character of the topography. Indeed, using single or few topographic features might lead in some cases to highly nonlinear $q - \psi$ relationships, not allowing to define a characteristic l_b. A possible cause of the nonlinear behaviour might be the strong loss of energy, since the theory is based on the rapid decay of enstrophy with respect to the slow decay of energy.

The comparison of shallow-water results with simulations based on quasi-geostrophy provides coincidences and differences that must be taken into account. At a first glance one observes qualitative similarities in the flow evolution for both cases (e.g. from vorticity plots), even for non-small topographic amplitudes. Some cautions must be taken, however, when this restriction is violated in quasi-geostrophic simulations. For instance, when using larger horizontal scales of the topography the qualitative resemblance between both cases might be less noticeable or even dissapear, as shown in figure 11. Quantitative differences can be observed in scatter plots, where the symmetry between positive and negative topographic perturbations is broken in the shallow-water formulation: flow over hills (anticyclonic) shows a more pronounced slope compared with the (cyclonic) structures over valleys. In contrast, scatter plots in the quasi-geostrophic case are more symmetrical. Another difference, although rather modest, is the faster energy decay in the shallow-water case. Summarizing, when studying quantitative measures in turbulent flows over abrupt topographies it is convenient to use the shallow-water formulation. For qualitative purposes, quasi-geostrophic results over this type of topography might still be useful.

The role of no-slip boundaries is to decrease the average length scale of the flow, which can be regarded as a slight disorganization of the flow. This effect is observed from vorticity fields, for instance. The essential mechanism is that no-slip conditions imply the formation of thin filaments near the walls that are rapidly dissipated (due to their short scale) thus implying a faster decay near the boundaries, and a general decrease of l. This is corroborated by comparing the evolution of integral quantities obtained with free-slip simulations, where l grows faster and reaches higher values than in the no-slip case.

REFERENCES

Adcock, S. & Marshall, D. P. 2000 Interactions between geostrophic eddies and the mean circulation over large-scale bottom topography. *J. Phys. Oceanogr.* **30**, 3223–3238.

Batchelor, G. K. 1969 Computation of the energy spectrum in homogeneous two-dimensional turbulence. *Phys. Fluids Suppl.* II **12**, 233–239.

Bretherton, F. P. & Haidvogel, D. B. 1976 Two-dimensional turbulence above topography. *J. Fluid Mech.* **78**, 129–154.

Carnevale, G. F. & Frederiksen, J. S. 1987 Nonlinear stability and statistical mechanics of flow over topography. *J. Fluid Mech.* **175**, 157–181.

Clercx, H. J. H., van Heijst, G. J. F., Molenaar, D. & Wells, M. G. 2005 No-slip walls as vorticity sources in two-dimensional bounded turbulence. *Dyn Atmos. Oceans* **40**, 3–21.

Clercx, H. J. H., Maassen, S. R. & van Heijst, G. J. F. 1999 Decaying two-dimensional turbulence in square containers with no-slip or stress-free boundaries. *Phys. Fluids* **11**, 611–626.

Grimshaw, R., Tang, Y. & Broutman, D. 1994 The effect of vortex stretching on the evolution of barotropic eddies over a topographic slope. *Geophys. Astrophys. Fluid Dyn.* **76**, 43–71.

van Heijst, G. J. F. & Clercx, H. J. H. 2009 Laboratory modelling of geophysical vortices. *Annu. Rev. Fluid Mech.* **41**, 143–164.

https://doi.org/10.1017/S0022112009991777 Published online by Cambridge University Press

Maassen, S. R., Clercx, H. J. H. & van Heijst, G. J. F. 2002 Self-organization of quasi-two-dimensional turbulence in stratified fluids in square and circular containers. *Phys. Fluids* **14**, 2150–2169.

Pedlosky, J. 1987 *Geophysical Fluid Dynamics*. Springer-Verlag.

Salmon, R., Holloway, G. & Hendershott, M. 1976 The equilibrium statistical mechanics of simple quasi-geostrophic models. *J. Fluid Mech.* **75**, 691–703.

Zavala Sansón, L. 2007 The long-time decay of rotating homogeneous flows over variable topography. *Dyn. Atmos. Oceans* **44**, 29–50.

Zavala Sansón, L. & van Heijst, G. J. F. 2002 Ekman effects in a rotating flow over bottom topography. *J. Fluid Mech.* **471**, 239–256.

Zavala Sansón, L. & Sheinbaum, J. 2008 Elementary properties of the enstrophy and strain fields in confined two-dimensional flows. *Eur. J. Mech.* B/*Fluids* **27**, 54–61.

https://doi.org/10.1017/S0022112009991777 Published online by Cambridge University Press